Journal of
Materials Chemistry A

Twist Angle has Weak Influence on Charge Separation and Strong Influence on Recombination in MoS2/WS2 Bilayer: Ab Initio Quantum Dynamics

Journal:	*Journal of Materials Chemistry A*
Manuscript ID	TA-ART-12-2021-010788.R1
Article Type:	Paper
Date Submitted by the Author:	14-Feb-2022
Complete List of Authors:	Zhu, Yonghao; Beijing University of Chemical Technology Fang, Wei-hai; Beijing Normal University, College of Chemistry Rubio, Angel; Max-Planck-Institut fur Struktur und Dynamik der Materie Long, Run; Beijing Normal University, College of Chemistry Prezhdo, Oleg; University of Southern California, Chemistry

Twist Angle has Weak Influence on Charge Separation and Strong Influence on Recombination in MoS_2/WS_2 Bilayer: Ab Initio Quantum Dynamics

Yonghao Zhu[1], Wei-Hai Fang[1], Angel Rubio[2], Run Long[1*], Oleg V. Prezhdo[3]

[1]*College of Chemistry, Key Laboratory of Theoretical & Computational Photochemistry of Ministry of Education, Beijing Normal University, Beijing, 100875, People's Republic of China*

[2]*Max Planck Institute for the Structure and Dynamics of Matter, 22761 Hamburg, Germany*

[3]*Departments of Chemistry, Physics and Astronomy, University of Southern California, Los Angeles, CA 90089, USA*

ABSTRACT: Van der Waals heterojunctions of two-dimensional transition-metal dichalcogenides are intensely investigated for multiple optoelectronics applications. Strong and adjustable interactions between layers can influence charge and energy flow that govern material performance. We report ab initio quantum molecular dynamics investigation of the influence of the bilayer twist angle on charge transfer and recombination in MoS_2/WS_2 heterojunctions, including high-symmetry 0° and 60° configurations, and low symmetry 9.43° and 50.57° structures with Moiré patterns. The twist angle modulates interlayer coupling, as evidenced by changes in the interlayer distance, electron-vibrational interactions, and spectral shifts in the out-of-plane vibrational frequencies. Occurring on a femtosecond timescale, the hole transfer depends weakly on the twist angle and is ultrafast due to high density of acceptor states and large nonadiabatic coupling. In contrast, the electron-hole recombination takes nanoseconds and varies by an order of magnitude depending on the twist angle. The recombination is slow because it occurs across a large energy gap. It depends on the twist angle

---

[*] Corresponding author, E-mail: runlong@bnu.edu.cn

because the nonadiabatic coupling is sensitive to the interlayer distance and overlap of electron and hole wavefunctions. The Moiré pattern systems exhibit weaker interlayer interaction, generating longer-lived charges. Both charge separation and recombination are driven by out-of-plane vibrational motions. The simulations rationalize the experimental results on the influence of the bilayer twist angle on the charge separation and recombination. The atomistic insights provide theoretical guidance for design of high-performance optoelectronic devices based on 2D van der Waals heterostructures.

Two-dimensional (2D) materials, such as graphene and transition-metal dichalcogenides (TMDs), have been attracting extensive interest for their unique properties in electronics, optics, and mechanics, including both monolayers and multilayers.[1-3] As a semiconductor alternative to graphene, TMDs have been studied widely in optoelectronic devices, such as photodetectors,[4] photovoltaic[5] and photocatalytic cells,[6] and light-emitting diodes.[7] Stacking of van der Waals heterostructures (vdWHs) composed of 2D materials without direct chemical bonding can show special physical and chemical properties, such as ultrafast transfer of charge carriers,[8, 9] formation of hot interlayer excitons[10] exhibiting prolonged lifetimes,[11] interlayer energy transfer,[12] and spin-valley locking giving rise to valleytronics.[13] vdWHs offer a promising platform for designing new generations of optoelectronic devices, and studying unique photophysical and photochemical processes.

TMD $M^aX^a_2/M^bX^b_2$ heterojunctions, with M^a/M^b=Mo, W and X^a/X^b=S, Se, form "staggered gap" type-II band alignment,[8, 10, 14, 15] implying that electrons and holes separate into different layers. Some other vdWHs based on TMDs or additional 2D materials also exhibit type-II band alignment and favor charge separation, such as MoS_2/PbI_2, WSe_2/ HfN_2, and C_6N_6/C_2N.[16-20] Using first-principles calculations, Torun et al.[15] predicted that the MoS_2/WS_2 and $MoSe_2/WSe_2$ vdWHs exhibit long-lived excitons following charge separation, as confirmed by time-domain spectroscopies.[11, 21] Chen et al.[10] reported that interlayer charge separation is much faster than intralayer recombination, justifying the assumption that intralayer recombination can be ignored.[14, 22, 23] Due to lower energy and stronger interlayer coupling,[24, 25] the highly symmetrical stacking is normally most stable in nature. However, artificially stacked junctions can exhibit many interesting phenomena, such as unconventional superconductivity in graphene superlattices,[26] twist-angle dependent interlayer coupling,[27] and Moiré potentials that influence exciton diffusion.[28] Choi et al.[29] found that interlayer exciton lifetimes increase by an order of magnitude as the TMD vdWHs twist angle is varied slightly from 1° to 3.5°. For a wider range of twist angles, 0°-30°, the interlayer electron-hole recombination time changed between 40 ps and 3 ns.[13] On the other hand, rapid charge transfer in the WS_2/WSe_2[30] and MoS_2/WSe_2[13] vdWHs is insensitive to the twist angle, as shown by femtosecond pump–probe spectroscopy. Density functional theory (DFT) has become an essential tool for the investigation of vdWHs, employed to explain the experimental phenomena,[11, 14] elucidate of the mechanisms of charge carrier separation and recombination,[23] and predict material properties.[31, 32] The static electronic structures of vdWHs have been studied using both the linear-scaling fragment method[33] and the traditional first-principles DFT.[34] First-principles modeling of charge carrier dynamics can be achieved by nonadiabatic molecular dynamics (NA-MD) based on time-dependent DFT (TD-DFT). Still rare due to high computational expense, such studies can provide critical insights into photoinduced processes, extending beyond the reach of experiments and phenomenological theories.

Herein, we investigate the twist angle dependent hole transfer and electron-hole recombination in MoS_2/WS_2 vdWHs using real-time TD-DFT combined with NA-MD. Focusing on symmetric systems with the 0° and 60° twist angles, and asymmetric structures with the 9.43° and 50.57° angles, we demonstrate type-II band alignment in all cases, with the valence band maximum (VBM) and conduction band minimum (CBM) of WS_2 lying above those of MoS_2. The superlattices of the twisted 9.43° and 50.57° structures show clear Moiré patterns. The interlayer coupling between MoS_2 and WS_2 is notably weaker in the Moiré pattern systems, in agreement with the experimental results[27, 30, 35-37] and previous calculations.[31-33, 38] The weaker interlayer coupling leads to an increased bilayer distance and a slight red-shift of the main signal in the electron-vibrational influence spectra. The twist angle also causes variations of the energy gaps for the charge transfer and recombination. The hole transfer gaps are larger and the electron-hole recombination gaps are smaller in the Moiré systems. According to the NA-MD simulations, the hole transfer times range from 235 fs to 253 fs, demonstrating weak angle dependence. This finding is rationalized by small variations in the NA coupling (NAC) and energy gaps for the hole transfer, which are further offset by changes in the hole acceptor density of states (DOS). The weak sensitivity of the hole transfer process to the bilayer twist angle agrees well with the experimental data.[13, 39] In contrast, the electron-hole recombination exhibits strong twist angle dependence. The charge recombination time in the 0° system is 2 ns, while it is 9 and 6 times longer in the 9.43° and 50.57° systems, respectively. The significant increase in the recombination time is attributed to the reduced NAC due to mismatch of electron and hole wavefunctions, and weakened interlayer interaction. Both hole transfer and electron-hole recombination are promoted by the interlayer A_{1g} vibration, which accepts the excess electronic energy released during the transitions. Only a few other modes couple weakly to the electronic subsystem, and as a result, electronic coherence is maintained for long time, compared to analogous processes in other types of materials.[40-51] The calculations are consistent with the time-resolved[13, 28, 29, 52] and Raman[8, 9, 25, 53] spectroscopies, and provide a detailed atomistic understanding of the experiments.

Trajectory surface hopping[54, 55] is a mixed quantum-classical method,[56-61] in which the electronic subsystem are treated quantum mechanically, while atomic motions are described (semi-)classically.[62-64] It is a general methodology for studying far-from-equilibrium quantum dynamics of complex systems. Prezhdo and co-workers combined[59, 60, 65] the methodology with time-dependent Kohn-Sham theory and applied the classical path approximation,[66] initiating studies of a variety of processes in condensed matter systems, including ultrafast charge transfer in heterojunctions,[14, 22, 23, 31, 32] and charge recombination in metal oxides,[67-69] TMDs,[70-72] other 2D materials,[73, 74] and metal halide perovskites, [40-45, 47, 48] showing good agreement with the corresponding experiments. The details of the methodology and implementation are described in the earlier publications.[57, 58, 75, 76]

The Vienna ab initio Simulation Package[77] (VASP) was used to perform the simulations, including electronic structure calculations, geometry optimization, adiabatic MD, and calculation of NACs.[78, 79] The Perdew-Burke-Ernzerhof (PBE) DFT functional[80] and the projector-augmented wave method[81] were employed to treat the electron-exchange correlation energy and to describe interactions between electrons and ion cores, respectively. The energy cutoff of the planewave basis was set to 500 eV. A Γ-centered 4×4×1 Monkhorst-Pack k-point mesh[81] was applied to optimize geometry, and 20 points were inserted into each highly symmetrical path of the Brillouin zone for the band structures calculations. The vdW interactions were described by the Grimme's DFT-D3 method[82] because it is generally used with TMDs heterojunctions[83-86] due to its good accuracy and low cost. The energy convergence criterion of the electronic self-consistent field was 10^{-5} eV for all calculations, and the structures were fully optimized until the ionic forces were less than 0.005 eV/Å. After the geometries were optimized, the structures were heated to 300 K by repeated velocity rescaling. Then, 4 ps adiabatic MD trajectories were obtained in the microcanonical ensemble with a 1fs time step. The subsequent NA-MD simulations were performed using the decoherence-induced surface hopping method.[58, 62]

In order to study the angle-resolved photoinduced carrier dynamics, the MoS_2/WS_2 heterojunctions with the twist angles of 0°, 9.43°, 50.57°, and 60° were built, ***Fig. 1***, using the methods discussed in the previous studies.[87, 88] Calculation of possible angles is described in the Supporting Information (SI). Generally, smaller twist angles require larger superlattices, ***Table S1***. The 0° and 60° angles correspond to 3R and 2H stacking with almost no mismatch between two single layers because the lattice constants of the MoS_2 (3.16 Å) and WS_2 (3.18 Å) single layers are almost identical and lattice angles are the same in both materials,[89, 90] respectively. It is beneficial for a more consistent comparison of the different systems to keep the size of the supercells similar for all structures. Therefore, the highly symmetrical systems, 0° and 60°, are constructed as a $\sqrt{37}*\sqrt{37}$ supercells containing 222 atoms, with the superlattice constant close to 2 nm. Following the nomenclature proposed by Yu et at.,[91] the high-symmetry stacking configurations 0°, ***Fig. 1a***, and 60°, ***Fig. 1d*** , are named as R_h^M and H_h^h, where M, X, h, R and H represent transition-metal site, chalcogen site, hexagon center, and rhombohedral and hexagonal bulk polytypes, respectively. Thus, the R_h^M nomenclature for the 0° system, indicates that the transition metal of the top layer, Mo, sits above the hexagonal center of the bottom layer, WS_2. A three-stage high-symmetry stacking motif plays a significant role in determining the properties of the 9.43°, ***Fig. 1b***, and 50.57°, ***Fig. 1c***, twist superlattices, owing to the inherent differences between the configurations.[34] The 9.43° system contains R_h^h, R_h^M, and R_h^X, black dotted lines in ***Fig. 1b***. These are different for the 50.57° system, H_h^h, H_h^M, and H_h^X, black dotted lines in ***Fig. 1c***. Distinct Moiré pattern can be seen in the larger supercells of the 9.43° and 50.57° systems, ***Fig. S1***.

The interlayer carrier dynamics, such as carrier transfer and electron-hole recombination across bilayers, are highly susceptible to the interlayer coupling.[9, 92, 93] The Raman spectra and DFT analyses have confirmed angle-dependent interlayer interaction in TMDs vdWHs.[22, 27, 38, 94, 95] The high-symmetry stacking structures, 0° (3R) and 60° (2H), have the shortest interlayer spacing, meaning stronger interlayer coupling.[25, 36, 95] Fractional twist angles increase the distance between bilayers, weakening the interaction between them. The distance between the two layers, defined as the distance between Mo and W in the MoS_2/WS_2 vdWHs, ranges from 6.04 Å to 6.31 Å at 0 K, as Moiré superlattices emerge, ***Table 1***, which is consistent with the previous studies.[24, 27, 37, 94, 95] Even though the average interlayer distances increase slightly at

300 K, the 9.43° and 50.57° twisted structures still have larger distances than the 3R and 2H structures. Therefore, the interlayer couplings for 9.43° and 50.57° are smaller than those for 0° and 60°. At both 0 K and 300 K, the distance between Mo and W is larger in the 60° system than the 0° system, indicating a weaker interaction. Generally, the weaker the interlayer interaction, the smaller the NAC that determines the timescales of the interlayer charge separation and recombination.

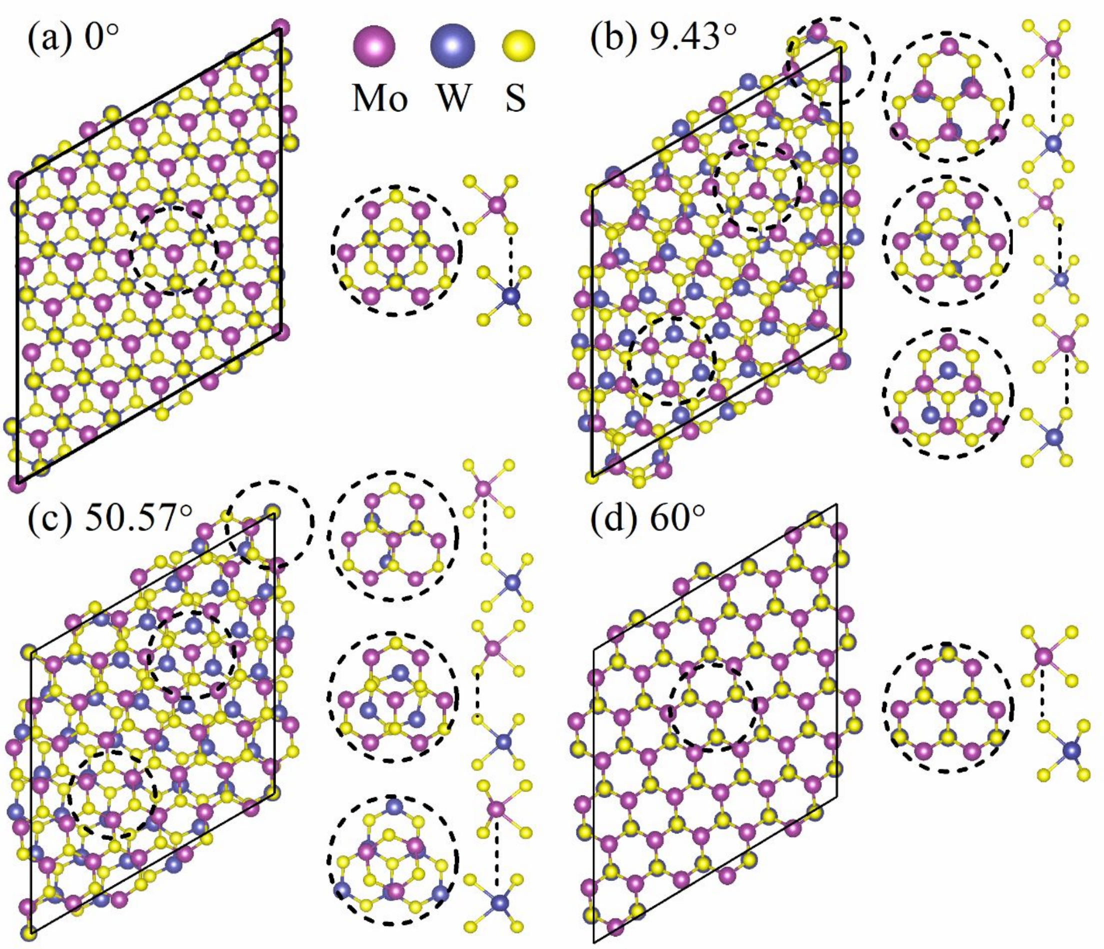

Figure 1. Atomic structures of the MoS_2/WS_2 vdWHs. The top and side views for **(a)** 0° (3R), **(b)** 9.43°, **(c)** 50.57°, and **(d)** 60° (2H). Panels (b) and (c) show unit cells. Panels (a) and (d) show supercells with the same number of atoms as in (b) and (c). Yellow, gray, and blue balls represent the S, W, and Mo elements, respectively. The images of the atomic structures were created with VESTA.[96]

Fig. 2 shows the band structures and the charge density distributions of the band edge states for the four MoS_2/WS_2 vdWHs at 0 K. ***Fig. S6*** shows the layer-projected DOS. Our results agree with the previous computations for the high-symmetry stacking systems, 0°, ***Fig. 2a***, and 60°, ***Fig. 2d***.[97-99] These band structures and DOS exhibit type-II alignments, ***Fig. S3***, indicating that the photoexcited electrons and holes are localized on different layers. In order to test the robustness of band alignment of 0^o and 60^o systems derived from the DFT-D3 method, we repeated the calculations of band structure and charge density of the MoS_2/WS_2 vdWHs constructed on the primitive cell using DFT-D3 and the more accurate and expensive optB88-vdW functional,[100, 101] **Fig. S4**. First, the band structure obtained by DFT-D3 is very similar to that calculated by optB88-vdW, showing type-II band alignment at the K points. Second, the shapes and distributions of the charge densities calculated by the two methods are also very similar. Third, the 60° structure has a larger bandgap than the 0° structure in both DFT-D3 (Figures S4a and S4c) and optB88-vdW (Figures S4b and S4d) calculations. The current work emphasizes relative differences between the various twisted systems, and the DFT-D3 method correctly reproduces these differences, as benchmarked against the more accurate optB88-vdW method. We prefer to use the cheap DFT-D3 method in the current work. Furthermore, the interlayer electric field induced by charge transfer can be ignored because of very small potential difference and marginal amount of charge transfer between two layers, evidenced by the calculate work functions and planar-averaged charge difference of the two systems (***Fig. S5***). By controlling pump wavelength to excite the electrons in the MoS_2 layer,[8, 39, 102, 103] one can initiate hole transfer from the MoS_2 layer into the WS_2 layer on a sub-picosecond timescale.[8, 103, 104] In contrast, the subsequent interlayer recombination of electron and hole takes place on a nanosecond timescale.[29, 53, 105, 106] Since the K-K recombination is faster than K-Γ and Q-Γ recombination because the latter two channels are momentum forbidden,[53] the current study focuses on the dominant K-K hole transfer and recombination, detailed in section S3 of SI. K-K exciton properties have been widely studied in TMD vdWHs.[53, 83, 91, 106] As described in section 2 of the SI, the K-point of the unit cell is folded into the K-point of the superlattice, ***Fig. S2***. Even though the Brillouin zones of the two layers twist in the k-space relative to each other, following the twist in the real space, ***Fig. S2d***, the K-points of the two layers in the superlattice are also folded to the K-point, ***Fig. 2c*** and ***2d***, which is consistent with the previous studies.[15, 99, 104] Therefore, the charge densities of the lower symmetry 9.43° and

50.57° twist systems are close to those of the higher symmetry 0° and 60° systems at the K-point. The differences in the stacking configurations leads to differences in the energy gaps for the charge separation and recombination. The gap for the hole transfer is the same in the 9.43° and 50.57° twist models (0.20 eV), however, it is larger than the gap for the 0° structure (0.11 eV) and smaller than the gap for the 60° structure (0.22 eV), ***Table 2***. All gaps are small, favoring fast hole transfer. The energy gap for the interlayer recombination is also the same for the Moiré pattern 9.43° and 50.57° models (1.57 eV). The gap for the 60° system is slightly bigger (1.58 eV), and the interlayer recombination gap for the 0° system is the largest (1.65 eV), ***Table 3***. The DOS indicates that WS_2 has a larger contribution to the VBM for the 60° angle than for the 0° angle, ***Fig. S6***. The same is true of the 9.43° and 50.57° systems. In general, our calculations agree with the pervious findings about the electronic structure properties at 0 K.[24]

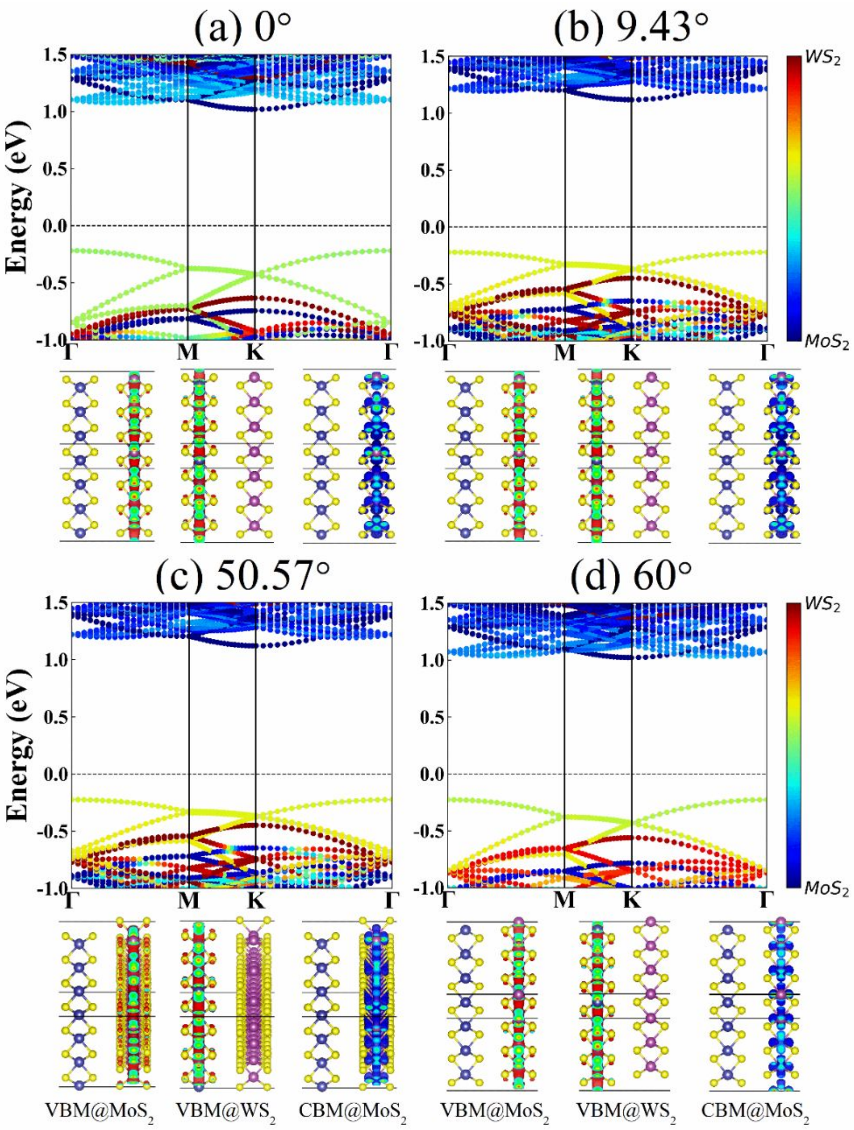

Figure 2. Band structures, and VBM and CBM charge densities of the **(a)** 0°, **(b)** 9.43°, **(c)** 50.57°, and **(d)** 60° systems. Post-processing of raw data was performed with VASPKIT.[107]

Table 1. Average Mo-W distance at 0 K and 300 K.

Twist Angle	0 K (Å)	300 K (Å)
0°	6.04	6.07
9.43°	6.31	6.32
50.57°	6.31	6.33
60°	6.07	6.12

Hole transfer from the MoS_2 to the WS_2 takes places once the MoS_2 is excited. ***Fig. 3a*** shows the hole transfer dynamics in the MoS_2/WS_2 junctions with different twisted angles. Exponential fit, $P(t) = 1 - \exp(-t/\tau)$, is used to obtain the time constants, and the results are listed in ***Table 2***. Hole transfer takes place on a 250 fs timescale in all systems, with variation of less than 20 fs. The ultrafast hole transfer is weakly dependent on the twist angle, in agreement with the ultrafast time-resolved spectroscopy data.[13, 39] The experimental times range between 50 fs and 100 fs,[8, 39] which is faster than our results. We can attribute the difference to neglect of explicit Coulomb interactions[104] in our calculations. Electron-electron correlation effect is included implicitly in the DFT functional. Explicit treatment of electron-hole interactions requires expensive GW plus Bethe-Salpeter methods. Nevertheless, the dependence of the carrier dynamics on the twist angle is correctly captured by the inexpensive and widely available PBE functional with large superlattices. The hole transfer in the current calculation is determined by the magnitude of the NAC, $-i\hbar\langle\Phi_j\left|\nabla_{\boldsymbol{R}}\right|\Phi_k\rangle \cdot d\boldsymbol{R}/dt$, which depends on the sensitivity of the initial and final wavefunctions to atomic motions. The NACs of the 0° and 60° systems are larger than the NAC of the 9.43° and 50.57° systems, because of the shorter interlayer distance and stronger interlayer coupling, ***Table 1***. However, the DOS at the VBM@WS_2 is larger in the 9.43°, 50.57°, and 60° systems than the 0° system, ***Fig. S6***, implying faster transfer. Overall, the hole transfer time is independent of the relative rotation of the two layers.

By performing the Fourier transforms (FT) of the unnormalized autocorrelation functions (ACFs) of energy gap fluctuations at 300 K, shown in ***Fig. S7***, we obtain the spectral density for hole transfer, ***Fig.3b***. The spectral density identifies the vibrational modes that couple to the electronic subsystem and accommodate the excess energy released during the hole transfer.[66] The height of the peak at a given frequency indicates the strength of electron-phono coupling to the corresponding vibrational mode. According to the Raman spectra, out-of-plane vibration for WS_2 and MoS_2 locate at 416 cm^{-1} and 404 cm^{-1}, respectively.[108] As illustrated in ***Fig. 3b***, the dominant vibration peaks are at about 400 cm^{-1} in all four systems, corresponding to the out-of-plane A_{1g} mode. [9, 25, 103] Weaker peaks appear around the main mode in the 60° structure. In particular, the lower frequency 342 cm^{-1} signal corresponds to the E_{2g} mode. The

50.57° Moiré pattern system contains a peak at 34 cm^{-1} corresponding to the layer breathing B_{2g} mode, which modulates interlayer distance and coupling. We spectral density analysis is surprisingly consistent with the experimental Raman spectra,[30, 39, 109, 110] even though the electron-vibrational coupling selection rules are different for the Raman spectrum and the hole transfer.

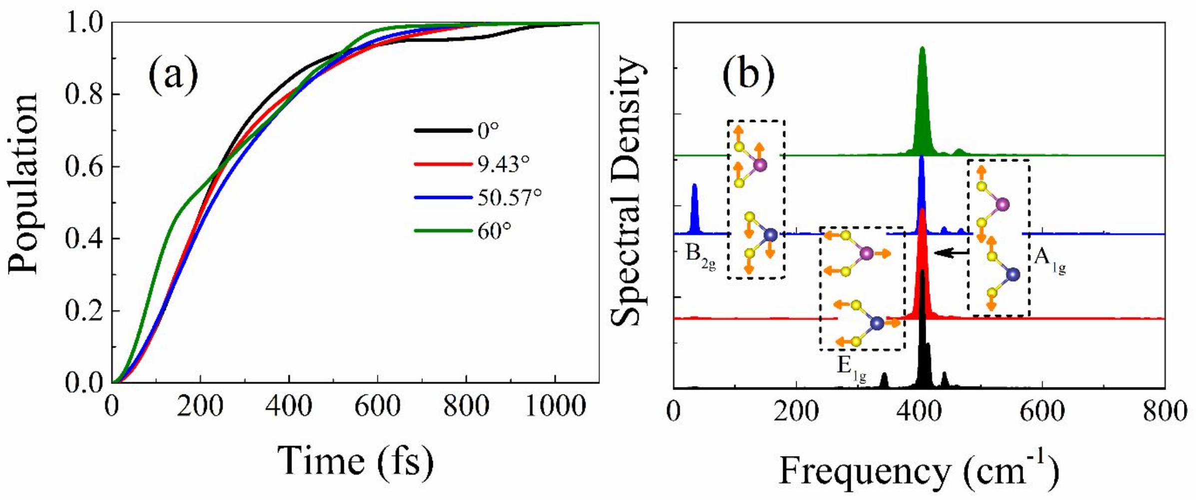

Figure 3. **(a)** Dynamics and **(b)** spectral densities for hole transfer in the 0°, 9.43°, 50.57°, and 60° structures. The inserts in (b) depict the key phonon modes. The spectral densities are obtained by Fourier transforms of ACFs of energy gap fluctuations.

Table 2. Energy gap, average absolute NAC, and time of hole transfer for the different twist angles.

Twist Angle	Gap (eV)	NAC (meV)	Hole Transfer Time (fs)
0°	0.11	1.82	235
9.43°	0.20	1.52	246
50.57°	0.20	1.57	250
60°	0.22	1.77	253

Following the hole transfer, the photoexcited electron localized inside MoS_2 recombines slowly with the hole in WS_2. ***Fig. 4*** demonstrates the nonradiative electron-hole interlayer recombination dynamics for all twisted MoS_2/WS_2 vdWHs. The decay rates and time constants,

τ, are listed in ***Table 3***. They are obtained by the short-time linear approximation to the exponential decay, $P(t) = \exp(-t/\tau) \approx 1 - t/\tau$, of the NA-MD population decay data shown in ***Fig. S8***. All correlation fitting coefficients are greater than 0.99. The nonradiative electron-hole recombination in the MoS_2/WS_2 junction with the 0° twist angle takes places within 1.93 ns, in agreement with the experimental data.[29, 53, 105, 106] The recombination slows down to 17.1 ns, 12.8 ns, and 7.72 ns for the 9.43°, 50.57°, and 60° twist angles, respectively. The differences in the electron-hole recombination times can be attributed to changes in the NAC between the CBM@MoS_2 and the VBM@WS_2, ***Table 3***. The NAC strength correlates with the interlayer distance, ***Table 3***. Weaker electron-vibrational NAC is caused by decoupling between the layers.[13, 28, 29, 52] The interlayer carrier recombination times are four orders of magnitude longer than the hole transfer times due to the factor of 8 larger energy gap, and the factor of 5-8 smaller NAC.

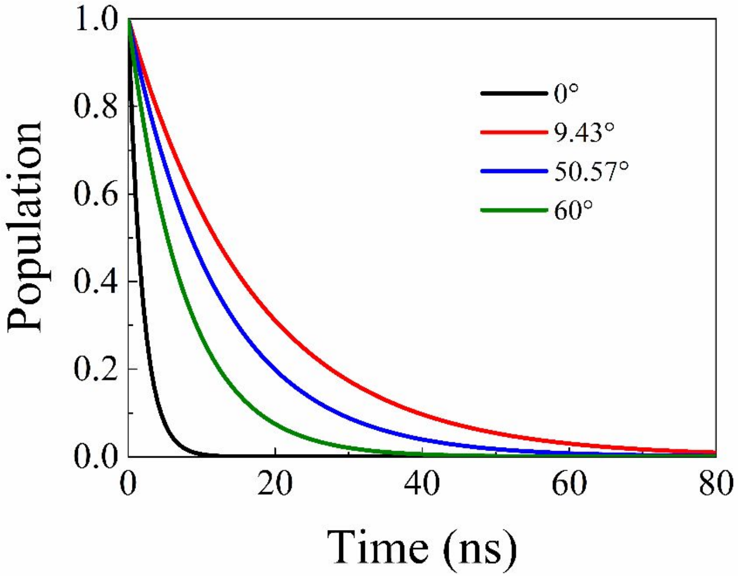

Figure 4. Nonradiative electron-hole recombination dynamics in the structures with the 0°, 9.43°, 50.57°, and 60° twist angles. Further data for the recombination dynamics are provided in ***Fig. 5***.

Similar to the hole transfer, the spectral densities can be obtained by performing FTs of the fluctuations of the energy gaps for the electron-hole recombination process. The spectra densities identify the phonon modes that promote the nonradiative relaxation and accept the energy released during the charge recombination. The spectra, shown in ***Fig. 5a***, contain two kinds of peaks located at 342 cm^{-1} and 404-440 cm^{-1}, corresponding to the E$_{1g}$ and A$_{1g}$ Raman active in-plane and out-of-plane vibrations,[25, 53] as shown schematically in the inserts. The strongest signal seen for the out-of-plane A$_{1g}$ mode indicates that the electron energy is dissipated initial to interlayer motions, and only later the energy flows into intralayer vibrations. Because bilayer twisting reducing the strength of the interlayer coupling, the out-of-plane vibrations become slightly red-shifted in the twisted structures, agreeing with the experiment data.[37, 109, 111] Further, the contributions of the E$_{1g}$ mode and the satellite peak just above the A$_{1g}$ mode weaken and disappear upon twisting, ***Fig. 5a***. Notably, the 9.43° and 50.57° asymmetric systems with Moiré patterns contain a signal at 34 cm^{-1} corresponding to the layer breathing B$_{2g}$ mode. The mode is activated due to reduced symmetry that relaxes electron-phonon coupling selection rules.

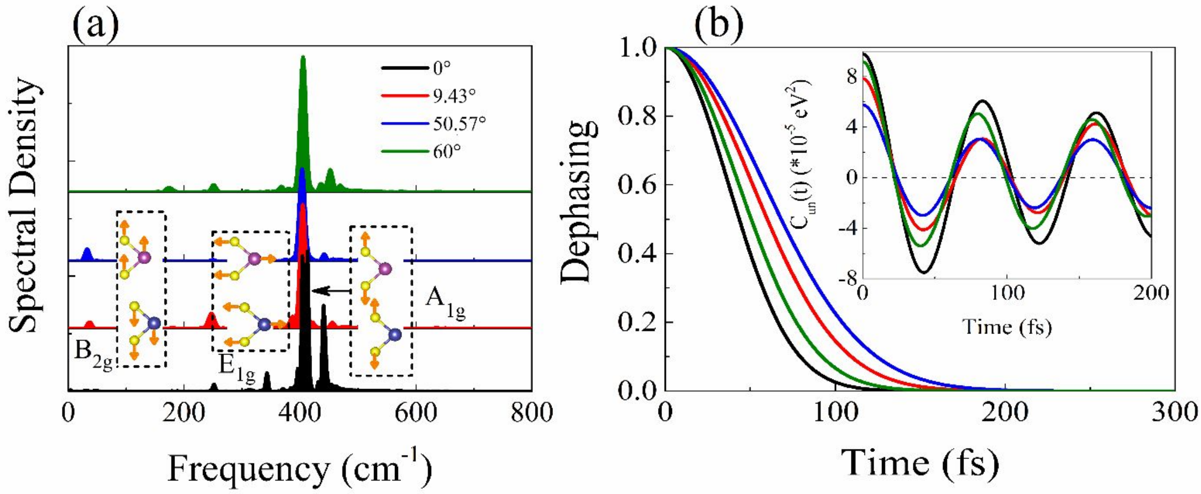

Figure 5. Electron-hole recombination. **(a)** Spectral densities calculated by Fourier transforms of ACFs of energy gap fluctuations. The inserts show phonon modes corresponding to the defected frequencies. **(b)** Pure-dephasing functions. The insert shows unnormalized ACFs.

Fig. 5b shows pure-dephasing functions, obtained from the energy gap ACFs using the second-order cumulant approximation in the optical response theory.[66, 112] The pure-dephasing functions characterize elastic electron-phono scattering that causes loss of the phase relation between the initial and final electronic states. The pure-dephasing functions are fitted with Gaussian, $\exp[-0.5(t/\tau)^2]$, and the pure-dephasing times are listed in ***Table 3***. Smaller pure-dephasing times indicate stronger electron-vibrational interactions. The highly symmetrical structures, 0° and 60°, show faster pure-dephasing than the 9.43° and 50.57° structure, indicating stronger interaction. Overall, the pure-dephasing times are quite long compared to other systems, such as semiconductor quantum dots[49-51] and metal halide perovskites, [40-48] because few phonon modes couple to the electronic subsystem, ***Fig.5a***. Typically, the pure-dephasing time is determined by the amplitude of the phonon-induced oscillation of the corresponding electronic energy gap.[66] The oscillation amplitude gives the initial value of the unnormalized ACF, shown in the insert of ***Fig. 5b***. Indeed, faster decay of the pure-dephasing functions correlates with the larger initial ACF value. The ACFs exhibit a prominent oscillation, corresponding to the A_{1g} mode frequency, and decay slowly because other modes couple to the electronic transition only weakly, ***Fig.5a***.

Table 3. Energy gap, average absolute NAC, pure-dephasing time, nonradiative electron-hole recombination rate and carrier lifetime for the different twist angles.

Twist Angle	Gap (eV)	NAC (meV)	Dephasing (fs)	Rate (ns^{-1})	Lifetime (ns)
0°	1.65	0.43	37	0.5171	1.93
9.43°	1.57	0.20	51	0.05838	17.13
50.57°	1.57	0.22	58	0.08077	12.38
60°	1.58	0.38	43	0.1296	7.72

In summary, we have employed real time TD-DFT and NA-MD to study photoinduced ultrafast hole transfer and nonradiative electron-hole recombination between bilayers in MoS_2/WS_2 vdWHs with several twist angles, 0°, 9.43°, 50.57°, and 60°. The 9.43° and 50.57° twisted structures exhibit distinct Moiré patterns. The 3R and 2H stacking structures, produced by the 0° and 60° angles, have been modeled using $\sqrt{37}*\sqrt{37}$ supercells that contain the same number of atoms as the 9.43° and 50.57° Moiré pattern models. The calculations indicate that the four vdWHs create type-II band alignment, in which the VBM and CBM of WS_2 have higher energies than the corresponding MoS_2 band edges. The interlayer coupling is significantly weakened in the asymmetric 9.43° and 50.57° stacking configurations, as reflected in the increased distance between the two layers and a slight red-shift of the out-of-plane vibration signals in the spectral densities. The hole transfer energy gaps are larger in the 9.43° and 50.57° than 0° and 60° systems, while the recombination gaps are smaller. The electronic structure and adiabatic MD results agree with experiments and previous calculations.

The ab initio quantum dynamics calculations demonstrate ultrafast hole transfer across the interface with 235 fs to 253 fs time constants. The transfer is ultrafast because the energy gaps between the initial and final states are small, the acceptor DOS are large, and the NAC is strong. The hole transfer time is weakly dependent on the twist angle because these properties change little with the angle, and the decreased NAC and increased gap in the non-0° structures are offset by the larger acceptor DOS. In contrast, the nonradiative electron-hole recombination is strongly sensitive to the twist angle. The recombination is faster in the symmetric 0° and 60° systems, and slower in the asymmetric 9.43° and 50.57° structures, with the timescales spanning an order of magnitude. The difference arises due to variation in the NAC that is sensitive to the interlayer distance and overlap of the initial and final wavefunctions. Our results rationalize experimental observations and demonstrate how the twist angle can be used to control charge recombination without affecting charge separation. This is the first ab initio quantum dynamics study of the influence of the twist angle on non-equilibrium electronic processes in 2D materials. Adjusting interactions between 2D layers provides an important handle for tuning performance of optoelectronic devices, such as photodetectors and solar cells.

Supporting Information. Construction of twisted bilayers, k-points unfolding, additional band structures, band structures and charge density derived from optB88-vdW functional, work functions and charge density differences obtained using DFT-D3method, layer projected densities of states, phonon-driven evolution of electronic state energies, NA-MD results and their fitting.

Notes

The authors declare no competing financial interest.

ACKNOWLEDGEMENTS

This work was supported by the National Natural Science Foundation of China, grant Nos.

21973006, 51861135101 and 21703222. R. L. acknowledges the Recruitment Program of Global Youth Experts of China and the Beijing Normal University Startup Package. O.V.P. acknowledges support of the US National Science Foundation, grant No. CHE-1900510.

REFERENCES

1. Z.-R. Chen, Y.-Q. Zhu, S.-M. Xu, Y. Zhao, Q. Peng and H. Yan, *J. Mater. Chem. A*, 2021, **9**, 20466-20482.
2. M. Ahmadi, O. Zabihi, S. Jeon, M. Yoonessi, A. Dasari, S. Ramakrishna and M. Naebe, *J. Mater. Chem. A*, 2020, **8**, 845-883.
3. L. Zhang, Z. Yang, T. Gong, R. Pan, H. Wang, Z. Guo, H. Zhang and X. Fu, *J. Mater. Chem. A*, 2020, **8**, 8813-8830.
4. D. Jiang, Z. Liu, Z. Xiao, Z. Qian, Y. Sun, Z. Zeng and R. Wang, *J. Mater. Chem. A*, 2022, **10**, 89-121.
5. M. Samadi, N. Sarikhani, M. Zirak, H. Zhang, H.-L. Zhang and A. Z. Moshfegh, *Nanoscale Horiz.*, 2018, **3**, 90-204.
6. A. Hasani, M. Tekalgne, Q. V. Le, H. W. Jang and S. Y. Kim, *J. Mater. Chem. A*, 2019, **7**, 430-454.
7. W. Yang, J. Shang, J. Wang, X. Shen, B. Cao, N. Peimyoo, C. Zou, Y. Chen, Y. Wang, C. Cong, W. Huang and T. Yu, *Nano Lett.*, 2016, **16**, 1560-1567.
8. X. Hong, J. Kim, S.-F. Shi, Y. Zhang, C. Jin, Y. Sun, S. Tongay, J. Wu, Y. Zhang and F. Wang, *Nat. Nanotechnol.*, 2014, **9**, 682-686.
9. S. Tongay, W. Fan, J. Kang, J. Park, U. Koldemir, J. Suh, D. S. Narang, K. Liu, J. Ji, J. Li, R. Sinclair and J. Wu, *Nano Lett.*, 2014, **14**, 3185-3190.
10. H. Chen, X. Wen, J. Zhang, T. Wu, Y. Gong, X. Zhang, J. Yuan, C. Yi, J. Lou, P. M. Ajayan, W. Zhuang, G. Zhang and J. Zheng, *Nat. Commun.*, 2016, **7**, 12512.
11. Z. Wang, P. Altmann, C. Gadermaier, Y. Yang, W. Li, L. Ghirardini, C. Trovatello, M. Finazzi, L. Duò, M. Celebrano, R. Long, D. Akinwande, O. V. Prezhdo, G. Cerullo and S. Dal Conte, *Nano Lett.*, 2021, **21**, 2165-2173.
12. D. Kozawa, A. Carvalho, I. Verzhbitskiy, F. Giustiniano, Y. Miyauchi, S. Mouri, A. H. Castro Neto, K. Matsuda and G. Eda, *Nano Lett.*, 2016, **16**, 4087-4093.
13. H. Zhu, J. Wang, Z. Gong, Y. D. Kim, J. Hone and X. Y. Zhu, *Nano Lett.*, 2017, **17**, 3591-3598.
14. L. Li, R. Long and O. V. Prezhdo, *Chem. Mater.*, 2017, **29**, 2466-2473.
15. E. Torun, H. P. C. Miranda, A. Molina-Sánchez and L. Wirtz, *Phys. Rev. B*, 2018, **97**, 245427.
16. M. K. Mohanta and A. De Sarkar, *Phys. Rev. B*, 2020, **102**, 125414.
17. S. Yuan, W. F. Io, J. Mao, Y. Chen, X. Luo and J. Hao, *ACS Applied Nano Materials*, 2020, **3**, 11979-11986.
18. Y. Ma, X. Zhao, T. Wang, W. Li, X. Wang, S. Chang, Y. Li, M. Zhao and X. Dai, *Phys. Chem. Chem. Phys.*, 2016, **18**, 28466-28473.
19. M. K. Mohanta, A. Rawat, N. Jena, Dimple, R. Ahammed and A. De Sarkar, *ACS Appl. Mater. Interfaces*, 2020, **12**, 3114-3126.
20. M. Mukherjee, R. Jana and A. Datta, *Phys. Chem. Chem. Phys.*, 2021, **23**, 3925-3933.
21. L. A. Jauregui, A. Y. Joe, K. Pistunova, D. S. Wild, A. A. High, Y. Zhou, G. Scuri, K. De Greve, A. Sushko, C.-H. Yu, T. Taniguchi, K. Watanabe, D. J. Needleman, M. D. Lukin, H. Park and P. Kim, *Science*, 2019, **366**, 870.
22. C. Zhang, C.-P. Chuu, X. Ren, M.-Y. Li, L.-J. Li, C. Jin, M.-Y. Chou and C.-K. Shih, *Sci. Adv.*, 2017, **3**, e1601459.
23. R. Long and O. V. Prezhdo, *Nano Lett.*, 2016, **16**, 1996-2003.
24. W. Yang, H. Kawai, M. Bosman, B. Tang, J. Chai, W. L. Tay, J. Yang, H. L. Seng, H. Zhu, H. Gong, H. Liu, K. E. J. Goh, S. Wang and D. Chi, *Nanoscale*, 2018, **10**, 22927-22936.
25. J. Zhang, J. Wang, P. Chen, Y. Sun, S. Wu, Z. Jia, X. Lu, H. Yu, W. Chen, J. Zhu, G. Xie, R. Yang, D.

Shi, X. Xu, J. Xiang, K. Liu and G. Zhang, *Adv. Mater.*, 2016, **28**, 1950-1956.

26. Y. Cao, V. Fatemi, S. Fang, K. Watanabe, T. Taniguchi, E. Kaxiras and P. Jarillo-Herrero, *Nature*, 2018, **556**, 43-50.
27. P. K. Nayak, Y. Horbatenko, S. Ahn, G. Kim, J.-U. Lee, K. Y. Ma, A. R. Jang, H. Lim, D. Kim, S. Ryu, H. Cheong, N. Park and H. S. Shin, *ACS Nano*, 2017, **11**, 4041-4050.
28. J. Choi, W.-T. Hsu, L.-S. Lu, L. Sun, H.-Y. Cheng, M.-H. Lee, J. Quan, K. Tran, C.-Y. Wang, M. Staab, K. Jones, T. Taniguchi, K. Watanabe, M.-W. Chu, S. Gwo, S. Kim, C.-K. Shih, X. Li and W.-H. Chang, *Sci. Adv.*, 2020, **6**, eaba8866.
29. J. Choi, M. Florian, A. Steinhoff, D. Erben, K. Tran, D. S. Kim, L. Sun, J. Quan, R. Claassen, S. Majumder, J. A. Hollingsworth, T. Taniguchi, K. Watanabe, K. Ueno, A. Singh, G. Moody, F. Jahnke and X. Li, *Phys. Rev. Lett.*, 2021, **126**, 047401.
30. K. Wang, B. Huang, M. Tian, F. Ceballos, M.-W. Lin, M. Mahjouri-Samani, A. Boulesbaa, A. A. Puretzky, C. M. Rouleau, M. Yoon, H. Zhao, K. Xiao, G. Duscher and D. B. Geohegan, *ACS Nano*, 2016, **10**, 6612-6622.
31. J. Zhang, H. Hong, C. Lian, W. Ma, X. Xu, X. Zhou, H. Fu, K. Liu and S. Meng, *Adv. Sci.*, 2017, **4**, 1700086.
32. J. Zhang, H. Hong, J. Zhang, H. Fu, P. You, J. Lischner, K. Liu, E. Kaxiras and S. Meng, *Nano Lett.*, 2018, **18**, 6057-6063.
33. J. Kang, J. Li, S.-S. Li, J.-B. Xia and L.-W. Wang, *Nano Lett.*, 2013, **13**, 5485-5490.
34. H. Guo, X. Zhang and G. Lu, *Sci. Adv.*, 2020, **6**, eabc5638.
35. A. A. Puretzky, L. Liang, X. Li, K. Xiao, B. G. Sumpter, V. Meunier and D. B. Geohegan, *ACS Nano*, 2016, **10**, 2736-2744.
36. H. Fang, C. Battaglia, C. Carraro, S. Nemsak, B. Ozdol, J. S. Kang, H. A. Bechtel, S. B. Desai, F. Kronast, A. A. Unal, G. Conti, C. Conlon, G. K. Palsson, M. C. Martin, A. M. Minor, C. S. Fadley, E. Yablonovitch, R. Maboudian and A. Javey, *Proc. Natl. Acad. Sci.*, 2014, **111**, 6198.
37. L. Wu, C. Cong, J. Shang, W. Yang, Y. Chen, J. Zhou, W. Ai, Y. Wang, S. Feng, H. Zhang, Z. Liu and T. Yu, *Nano Res.*, 2021, **14**, 2215-2223.
38. W. T. Geng, V. Wang, J. B. Lin, T. Ohno and J. Nara, *J. Phys. Chem. C*, 2021, **125**, 1048-1053.
39. Z. Ji, H. Hong, J. Zhang, Q. Zhang, W. Huang, T. Cao, R. Qiao, C. Liu, J. Liang, C. Jin, L. Jiao, K. Shi, S. Meng and K. Liu, *ACS Nano*, 2017, **11**, 12020-12026.
40. W. Li, Y.-Y. Sun, L. Li, Z. Zhou, J. Tang and O. V. Prezhdo, *J. Am. Chem. Soc.*, 2018, **140**, 15753-15763.
41. J. He, W.-H. Fang, R. Long and O. V. Prezhdo, *ACS Energy Lett.*, 2018, **3**, 2070-2076.
42. J. He, W.-H. Fang and R. Long, *Chem. Sci.*, 2019, **10**, 10079-10088.
43. Z. Zhang and R. Long, *J. Phys. Chem. Lett.*, 2019, **10**, 3433-3439.
44. W. Li, Y. She, A. S. Vasenko and O. V. Prezhdo, *Nanoscale*, 2021, **13**, 10239-10265.
45. Y. Wu, W. Chu, A. S. Vasenko and O. V. Prezhdo, *J. Phys. Chem. Lett.*, 2021, **12**, 8699-8705.
46. J. He, A. S. Vasenko, R. Long and O. V. Prezhdo, *J. Phys. Chem. Lett.*, 2018, **9**, 1872-1879.
47. R. Shi, A. S. Vasenko, R. Long and O. V. Prezhdo, *J. Phys. Chem. Lett.*, 2020, **11**, 9100-9109.
48. Z. Zhang, W.-H. Fang, M. V. Tokina, R. Long and O. V. Prezhdo, *Nano Lett.*, 2018, **18**, 2459-2466.
49. J. Liu, S. V. Kilina, S. Tretiak and O. V. Prezhdo, *ACS Nano*, 2015, **9**, 9106-9116.
50. R. Long, N. J. English and O. V. Prezhdo, *J. Am. Chem. Soc.*, 2013, **135**, 18892-18900.
51. R. Long, N. J. English and O. V. Prezhdo, *J. Phys. Chem. Lett.*, 2014, **5**, 2941-2946.
52. V. Kravtsov, A. D. Liubomirov, R. V. Cherbunin, A. Catanzaro, A. Genco, D. Gillard, E. M. Alexeev,

T. Ivanova, E. Khestanova, I. A. Shelykh, A. I. Tartakovskii, M. S. Skolnick, D. N. Krizhanovskii and I. V. Iorsh, *2D Mater.*, 2021, **8**, 025011.

53. M. Okada, A. Kutana, Y. Kureishi, Y. Kobayashi, Y. Saito, T. Saito, K. Watanabe, T. Taniguchi, S. Gupta, Y. Miyata, B. I. Yakobson, H. Shinohara and R. Kitaura, *ACS Nano*, 2018, **12**, 2498-2505.
54. M. Barbatti, *Wiley Interdiscip. Rev. Comput. Mol. Sci.*, 2011, **1**, 620-633.
55. J. C. Tully, *J. Chem. Phys.*, 2012, **137**, 22A301.
56. R. Crespo-Otero and M. Barbatti, *Chem. Rev.*, 2018, **118**, 7026-7068.
57. A. V. Akimov and O. V. Prezhdo, *J. Chem. Theory Comput.*, 2013, **9**, 4959-4972.
58. A. V. Akimov and O. V. Prezhdo, *J. Chem. Theory Comput.*, 2014, **10**, 789-804.
59. C. F. Craig, W. R. Duncan and O. V. Prezhdo, *Phys. Rev. Lett.*, 2005, **95**, 163001.
60. G. Zhou, G. Lu and O. V. Prezhdo, *Nano Lett.*, 2021, **21**, 756-761.
61. B. Wang, W. Chu, A. Tkatchenko and O. V. Prezhdo, *J. Phys. Chem. Lett.*, 2021, **12**, 6070-6077.
62. H. M. Jaeger, S. Fischer and O. V. Prezhdo, *J. Chem. Phys.*, 2012, **137**, 22A545.
63. P. Nijjar, J. Jankowska and O. V. Prezhdo, *J. Chem. Phys.*, 2019, **150**, 204124.
64. O. V. Prezhdo, *Theor. Chem. Acc.*, 2006, **116**, 206-218.
65. S. A. Fischer, B. F. Habenicht, A. B. Madrid, W. R. Duncan and O. V. Prezhdo, *J. Chem. Phys.*, 2011, **134**, 024102.
66. A. V. Akimov and O. V. Prezhdo, *J. Phys. Chem. Lett.*, 2013, **4**, 3857-3864.
67. L. Zhang, Q. Zheng, Y. Xie, Z. Lan, O. V. Prezhdo, W. A. Saidi and J. Zhao, *Nano Lett.*, 2018, **18**, 1592-1599.
68. W. Stier, W. R. Duncan and O. V. Prezhdo, *Adv. Mater.*, 2004, **16**, 240-244.
69. Z. Zhou, J. Liu, R. Long, L. Li, L. Guo and O. V. Prezhdo, *J. Am. Chem. Soc.*, 2017, **139**, 6707-6717.
70. X. Wang and R. Long, *J. Phys. Chem. Lett.*, 2020, **11**, 4086-4092.
71. L. Li, R. Long, T. Bertolini and O. V. Prezhdo, *Nano Lett.*, 2017, **17**, 7962-7967.
72. L. Li, M.-F. Lin, X. Zhang, A. Britz, A. Krishnamoorthy, R. Ma, R. K. Kalia, A. Nakano, P. Vashishta, P. Ajayan, M. C. Hoffmann, D. M. Fritz, U. Bergmann and O. V. Prezhdo, *Nano Lett.*, 2019, **19**, 6078-6086.
73. R. Long, W. Fang and A. V. Akimov, *J. Phys. Chem. Lett.*, 2016, **7**, 653-659.
74. Y. Wei and R. Long, *J. Phys. Chem. Lett.*, 2018, **9**, 3856-3862.
75. A. V. Akimov, *J. Comput. Chem.*, 2016, **37**, 1626-1649.
76. S. Pal, D. J. Trivedi, A. V. Akimov, B. Aradi, T. Frauenheim and O. V. Prezhdo, *J. Chem. Theory Comput.*, 2016, **12**, 1436-1448.
77. G. Kresse and J. Furthmüller, *Phys. Rev. B*, 1996, **54**, 11169-11186.
78. W. Chu and O. V. Prezhdo, *J. Phys. Chem. Lett.*, 2021, **12**, 3082-3089.
79. W. Chu, Q. Zheng, A. V. Akimov, J. Zhao, W. A. Saidi and O. V. Prezhdo, *J. Phys. Chem. Lett.*, 2020, **11**, 10073-10080.
80. J. P. Perdew, K. Burke and M. Ernzerhof, *Phys. Rev. Lett.*, 1996, **77**, 3865-3868.
81. P. E. Blöchl, *Phys. Rev. B*, 1994, **50**, 17953-17979.
82. S. Grimme, J. Antony, S. Ehrlich and H. Krieg, *J. Chem. Phys.*, 2010, **132**, 154104.
83. R. Gillen and J. Maultzsch, *Phys. Rev. B*, 2018, **97**, 165306.
84. Z. Zhou, X. Zhang, Y. Guo, Y. Zhang, X. Niu, L. Ma and J. Wang, *Phys. Rev. B*, 2021, **103**, 245411.
85. N. A. Pike, A. Dewandre, F. Chaltin, L. Garcia Gonzalez, S. Pillitteri, T. Ratz and M. J. Verstraete, *Phys. Rev. B*, 2021, **103**, 235307.
86. C. Long, Y. Dai, Z.-R. Gong and H. Jin, *Phys. Rev. B*, 2019, **99**, 115316.

87. M. R. Rosenberger, H.-J. Chuang, M. Phillips, V. P. Oleshko, K. M. McCreary, S. V. Sivaram, C. S. Hellberg and B. T. Jonker, *ACS Nano*, 2020, **14**, 4550-4558.
88. J. M. B. Lopes dos Santos, N. M. R. Peres and A. H. Castro Neto, *Phys. Rev. Lett.*, 2007, **99**, 256802.
89. Y. Yu, S. Hu, L. Su, L. Huang, Y. Liu, Z. Jin, A. A. Purezky, D. B. Geohegan, K. W. Kim, Y. Zhang and L. Cao, *Nano Lett.*, 2015, **15**, 486-491.
90. H.-P. Komsa and A. V. Krasheninnikov, *Phys. Rev. B*, 2013, **88**, 085318.
91. H. Yu, G.-B. Liu and W. Yao, *2D Mater.*, 2018, **5**, 035021.
92. S. Sim, D. Lee, J. Lee, M. Cha, S. Cha, W. Heo, S. Cho, W. Shim, K. Lee, J. Yoo, R. P. Prasankumar, H. Choi and M.-H. Jo, *Phys. Rev. B*, 2020, **101**, 174309.
93. P. Narang, L. Zhao, S. Claybrook and R. Sundararaman, *Adv. Opt. Mater.*, 2017, **5**, 1600914.
94. W. Yan, L. Meng, Z. Meng, Y. Weng, L. Kang and X.-a. Li, *J. Phys. Chem. C*, 2019, **123**, 30684-30688.
95. K. Liu, L. Zhang, T. Cao, C. Jin, D. Qiu, Q. Zhou, A. Zettl, P. Yang, S. G. Louie and F. Wang, *Nat. Commun.*, 2014, **5**, 4966.
96. K. Momma and F. Izumi, *J. Appl. Crystallogr.*, 2011, **44**, 1272-1276.
97. E. Torun, H. P. C. Miranda, A. Molina-Sánchez and L. Wirtz, *Phys. Rev. B*, 2018, **97**, 245427.
98. K. Kośmider and J. Fernández-Rossier, *Phys. Rev. B*, 2013, **87**, 075451.
99. Q. Zheng, Y. Xie, Z. Lan, O. V. Prezhdo, W. A. Saidi and J. Zhao, *Phys. Rev. B*, 2018, **97**, 205417.
100. J. Klimeš, D. R. Bowler and A. Michaelides, *J. Phys.: Condens. Matter*, 2009, **22**, 022201.
101. J. Klimeš, D. R. Bowler and A. Michaelides, *Phys. Rev. B*, 2011, **83**, 195131.
102. F. Ceballos, M. Z. Bellus, H.-Y. Chiu and H. Zhao, *ACS Nano*, 2014, **8**, 12717-12724.
103. H. Wang, J. Bang, Y. Sun, L. Liang, D. West, V. Meunier and S. Zhang, *Nat. Commun.*, 2016, **7**, 11504.
104. J. Liu, X. Zhang and G. Lu, *Nano Lett.*, 2020, **20**, 4631-4637.
105. J. Kiemle, F. Sigger, M. Lorke, B. Miller, K. Watanabe, T. Taniguchi, A. Holleitner and U. Wurstbauer, *arXiv reprints*, 2018, arXiv:1812.10697.
106. B. Miller, A. Steinhoff, B. Pano, J. Klein, F. Jahnke, A. Holleitner and U. Wurstbauer, *Nano Lett.*, 2017, **17**, 5229-5237.
107. V. Wang, N. Xu, J.-C. Liu, G. Tang and W.-T. Geng, *Comput. Phys. Commun.*, 2021, **267**, 108033.
108. C. Lee, H. Yan, L. E. Brus, T. F. Heinz, J. Hone and S. Ryu, *ACS Nano*, 2010, **4**, 2695-2700.
109. M. Liao, Z. Wei, L. Du, Q. Wang, J. Tang, H. Yu, F. Wu, J. Zhao, X. Xu, B. Han, K. Liu, P. Gao, T. Polcar, Z. Sun, D. Shi, R. Yang and G. Zhang, *Nat. Commun.*, 2020, **11**, 2153.
110. M. Baranowski, A. Surrente, L. Klopotowski, J. M. Urban, N. Zhang, D. K. Maude, K. Wiwatowski, S. Mackowski, Y. C. Kung, D. Dumcenco, A. Kis and P. Plochocka, *Nano Lett.*, 2017, **17**, 6360-6365.
111. A. M. van der Zande, J. Kunstmann, A. Chernikov, D. A. Chenet, Y. You, X. Zhang, P. Y. Huang, T. C. Berkelbach, L. Wang, F. Zhang, M. S. Hybertsen, D. A. Muller, D. R. Reichman, T. F. Heinz and J. C. Hone, *Nano Lett.*, 2014, **14**, 3869-3875.
112. S. Mukamel and S. Mukamel, *Principles of Nonlinear Optical Spectroscopy*, Oxford University Press, 1995.